A rapid and scalable method for making mixed metal oxide alloys for enabling accelerated materials discovery

Babajide Patrick Ajayi
Department of Chemical Engineering, University of Louisville, Louisville, Kentucky 40292, USA; and Conn Center for Renewable Energy Research, University of Louisville, Louisville, Kentucky 40292, USA

Sudesh Kumari
Conn Center for Renewable Energy Research, University of Louisville, Louisville, Kentucky 40292, USA

Daniel Jaramillo-Cabanzo
Department of Chemical Engineering, University of Louisville, Louisville, Kentucky 40292, USA; and Conn Center for Renewable Energy Research, University of Louisville, Louisville, Kentucky 40292, USA

Joshua Spurgeon and Jacek Jasinski
Conn Center for Renewable Energy Research, University of Louisville, Louisville, Kentucky 40292, USA

Mahendra Sunkara[a)]
Department of Chemical Engineering, University of Louisville, Louisville, Kentucky 40292, USA; and Conn Center for Renewable Energy Research, University of Louisville, Louisville, Kentucky 40292, USA

(Received 8 December 2015; accepted 23 February 2016)

The synthesis technique that can be used to accelerate the discovery of materials for various energy conversion and storage applications is presented. Specifically, this technique allows a rapid and controlled synthesis of mixed metal oxide particles using plasma oxidation of liquid droplets containing mixed metal precursors. The conventional wet chemical methods for synthesis of multimetal oxide solid solutions often require time-consuming high pressure and temperature processes, and so the challenge is to develop rapid and scalable techniques with precise compositional control. The concept is demonstrated by synthesizing binary and ternary transition metal oxide solid solutions with control over entire composition range using metal precursor solution droplets oxidized using atmospheric oxygen plasma. The results show the selective formation of metastable spinel and the rocksalt solid solution phases with compositions over the entire range by tuning the metal precursor composition. The synthesized manganese doped nickel ferrite nanoparticles, $NiMn_zFe_{2-z}O_4$ ($0 \leq z \leq 1$), exhibits considerable electrocatalytic activity toward oxygen evolution reaction, achieving an overpotential of 0.39 V at a benchmarking current density of 10 mA/cm^2 for a low manganese content of $z = 0.20$.

I. INTRODUCTION

Many grand challenges in energy conversion and storage need discovery of new materials.[1] However, there are not too many reported synthesis approaches that could easily be implemented for screening and rational understanding of structure–behavior relationships. Specifically, the challenges include semiconductors for photoelectrochemical water splitting,[2] stable electrocatalysts for oxygen evolution and reduction[3] and nitrogen reduction,[4] and for many heterogeneous gas–solid reactions including carbon dioxide reduction.[2] Many of the above challenges require synthesis of multielement solid solutions with composition over entire range regardless of phases present.

The conventional synthesis method is a solid state route that involves the mechanical milling of oxides, carbonates or nitrates.[5] Solid state route is highly unfavorable because it requires long processing time and elevated temperature and pressure.[6] Consequently, wet chemical methodologies, such as sol–gel,[7] co-precipitation[8] solvothermal techniques,[9] pyrolysis in air,[10] have all been proposed to deal with this problem. However, these methods require prolonged heat treatments and therefore are primarily restricted to equilibrium phases.[11] Besides, they are also low yield methods and involve multistep and laborious processes, each bearing a risk of introducing impurities to the final product. More so, with these methods, it is quite a challenge to control the size and composition of mixed metal oxide nanoparticles, a key parameter for the properties and performance of these materials.

So, there have been concerted efforts to make mixed metal oxide in a single step from inexpensive materials with high scalability and control over size and final

Contributing Editor: Artur Braun
[a)]Address all correspondence to this author.
e-mail: mahendra@louisville.edu
DOI: 10.1557/jmr.2016.92

 © Materials Research Society 2016

https://doi.org/10.1557/jmr.2016.92 Published online by Cambridge University Press

product composition, by using the flame spray pyrolysis (FSP) methods such as vapor-fed FSP,[12] liquid-fed FSP[13,14] and liquid-fed flame assisted spray pyrolysis.[15] Unfortunately, metal oxides produced through vapor-fed spray pyrolysis are limited to few oxides such as zirconium, aluminum, titanium, and silicon based oxides.[12] In addition, the starting materials of this synthesis route are basically volatile chlorides that release by-products such as hydrogen chloride gas which are not benign from the environmental perspective. Vapor-fed FSP has been improved upon by the incorporation of a liquid feed system,[12] making the process cleaner and has been shown with many metal oxides. Both liquid-fed flame assisted and FSP use either the enthalpy of combustion of precursors or external high enthalpy value flame for providing temperatures up to 2800 K.[16] Earlier works on combinatorial synthesis have used pyrolysis in air to convert precursor to mixed metal oxides, but have failed to show strong evidence that solid solutions are really formed.[10,17] Many of these techniques have only demonstrated to produce certain stable phases of mixed metal oxide solid solutions. However, it is crucial to be able to synthesize mixed metal oxide solid solutions over complete range of compositions for discovering new materials and for addressing grand challenges in energy conversion and storage.

So, here, a concept on the use of plasma oxidation involving mixed solution precursors is investigated. The liquid droplets are sprayed into high energy oxygen plasma where they react to form an oxidized solid powder. Earlier studies using plasma oxidation schemes have shown ultrafast timescales for both molten metals[18] and also metal oxides in the presence of alkali salts. Studies involving inductively coupled plasma for droplet-to-particle concept have been successful but only shown with single component.[19,20] Recently, Schaefer and co-workers[21] studied the gas phase nucleation and in vacuo deposition of iron oxide nanoparticles from ferrocene vapor in a microplasma reactor. The difficulties inherent in vapor phase nucleation are lack of precise compositional control in making multimetal oxides. While there are few studies on synthesis of mixed metal oxides by plasma oxidation of liquid droplets,[22,23] none to the best of our knowledge has demonstrated the compositional tuning capability of this method. Ultrafast timescales expected with plasma oxidation using oxygen radicals can inhibit steady state diffusion associated with equilibrium phase formation and thus leading to metastable phases such as solid solutions with varying composition over the entire range.

Specifically in this paper, the synthesis of mixed transition metal oxide comprising of binary metal oxides (nickel–manganese oxide, nickel–iron oxide) and ternary mixed metal oxides (involving nickel, manganese, and iron) have been demonstrated with exceptional control over composition and phases. To understand the functional behavior of these synthesized materials, we tested the activity of the above nanoparticles as an electrocatalyst for oxygen evolution reaction (OER). The OER, $2H_2O \rightarrow 4H^+ + O_2 + 4e^-$ (acidic solution) or $4OH^- \rightarrow 2H_2O + O_2 + 4e^-$ (basic solution), is heavily reliant on efficient electrocatalysts because it is kinetically sluggish and thus constitutes an outlet for efficiency loss and places a significant overpotential requirement in water splitting reactions.[24,25] Cogent understanding of the structural morphology and composition of catalysts at a molecular level has been instrumental in the rational design of robust electrocatalysts with high activities. The state-of-the-art OER electrocatalysts like RuO_x, IrO_x, and Pt are quite expensive; hence, it is important to find low-cost and readily available alternatives. High-throughput materials synthesis and screening have recently been used to find these alternatives, and the oxides of first row transition metals like nickel, iron, and cobalt have been reported to be good candidates.[26,27]

II. EXPERIMENTAL

A. Synthesis and electrode preparation

Experiments on precursor liquid droplet oxidation were performed using a homemade atmospheric microwave plasma flame reactor. There are two different reactor configurations: upstream and downstream [refer to Supplementary information Figs. S1(a) and S1(b)]. In the first design, the plasma flame is oriented vertically in such a way that the tip of the jet is pointing upward, whereas in the second design, the tip of the jet points vertically downward. While the first design is convenient for thin film deposition on substrates, the second design is especially useful where fairly large amounts of ultrafine mixed metal oxide powders are needed. In the downstream plasma configuration, compressed air and precursor liquid are forced through the nozzle of an atomizer creating liquid droplets of the precursor of an average size of ~5 μm that are transformed in mixed metal oxides as they pass through the plasma flame. Converted nanoparticle powder is directed by the vacuum pump into the air filter, where the powder is collected.

The electrodes were prepared by using the upstream plasma jet configuration. The precursor solutions were prepared using mixtures of nickel, iron, and manganese nitrates in desired proportion. Chemically pure grade of nickel(II) nitrate hexahydrate, manganese(II) nitrate hydrate, and iron(II) nitrate nonhydrate (research grade, Sigma Aldrich, St. Louis, Missouri) were used as starting materials without further purification. Appropriate amount of the precursors was weighed out and dissolved in deionized (DI) water to make up 1 M solution. About ~0.1 mL of prepared metal precursor solution was sprayed onto 2 cm^2 fluorine-doped tin-oxide (FTO)

https://doi.org/10.1557/jmr.2016.92 Published online by Cambridge University Press

coated glass substrates (Hartford Glass, Hartford, Connecticut) which were exposed to the upstream plasma jet with an input power of 500 W and a volumetric flow of 2 standard liters per minute (slpm) Ar, 11 slpm air, for 30 s. The argon gas is only necessary for plasma ignition, and is turned off after obtaining a stable plasma. The substrate temperature is measured using a pyrometer and is determined to be anywhere between 500 and 550 °C. The catalyst adhered very well to the surface of the substrate forestalling any use of a surfactant. The plasma power was set in such a way that the temperature of the substrate did not exceed 550 °C. The maximum temperature of 550 °C is set by the thermal stability of FTO-coated glass substrates, and the choice of FTO-coated glass substrates is based on its poor electrocatalytic properties. Substrates were cleaned prior to deposition by ultrasonication in an alkaline aqueous solution, deionized water, ethanol, and DI water for 10 min/step.

B. Material characterization

The morphology of the nickel–manganese oxide nanoparticles was characterized using a FEI Nova 600 NanoLab scanning electron microscope (SEM; FEI Company, Eindhoven, The Netherlands). A Bruker D8 powder x-ray diffraction (XRD; Bruker Corporation, Billerica, Massachusetts) system was used for crystal phase analysis. The data were processed to analyze sample $NiMn_{0.2}Fe_{1.8}O_4$ using FullProf.2k (Version 4.30—April, 2008-ILL JRC) in the Rietveld method for structure refinement. Program refinement of the first samples was started with the space group $Fd\bar{3}m$, origin at $\bar{3}m$, O in $32e^-$, A site in 8*f*, and B site in 16*c*. In the first step, the global parameters, such as 2θ-zero and background, were refined. In the next step, the structural parameters, such as lattice parameter, atomic coordinates, and site occupancy, were refined. High-resolution transmission electron microscopy (HRTEM), selected area electron diffraction (SAED) and nanoprobe-based energy dispersive x-ray spectroscopy (EDX) measurements were conducted using a FEI Tecnai F20 transmission electron microscope (TEM).

C. Electrochemical measurements

All the measurements were done in a three electrode setup equipped with SP-100 (Bio-Logic SAS, Claix, France). A saturated calomel electrode (SCE) was used as reference electrode. All potentials were converted and referred to the reversible hydrogen electrode (RHE) using the Nernst equation:

$$E_{RHE} = E_{SCE} + 0.241 + 0.059\text{pH} \quad . \qquad (1)$$

All measurements were performed in 1 M NaOH solution. The uncompensated resistance (R_u) of the cell was measured with single point high frequency impedance measurement, and current solution resistance (IR) drop was compensated at 85% through positive feedback using bio-logic EC-lab software. Our typical electrochemical cell had internal resistance, R_u around 20–25 Ω in 1 M NaOH.

III. RESULTS AND DISCUSSION

Experiments were conducted using several binary and ternary systems and the results are analyzed with various techniques to confirm that the composition of resulting solid solutions can be tuned over entire ranges. In fact, the data show complete tunability with respect to compositional control using precursor composition in liquid droplets. Specifically, the results with nickel and manganese oxides for binary systems and nickel, manganese and iron oxide solid solutions for ternary systems are illustrated. In addition, the resulting ternary solid solutions are investigated for their performance as electrocatalysts for OER.

A. Nickel–manganese oxide ($Ni_xMn_{1-x}O_y$)

The mixed metal oxide is in general represented by $Ni_xMn_{1-x}O_y$ where $0.0 \le x \le 1.0$ and y are dependent on the type of phase present. Throughout the full range of composition, $0.0 \le x \le 1.0$, the phase(s) present depends mainly on the x composition in the sample. Two clear phase regimes can be identified from XRD: (i) solid solution of $Ni_kMn_{1-k}O$ ($0.9 < x \le 1$) (ii) a solid solution of $Ni_mMn_{3-m}O_4$ ($0.05 < x \le 0.9$), where the indices k and m defines the rock-salt and spinel solid solution series, respectively. In the entire range, there is no segregation of NiO and MnO_x phases as evidenced by the absence of clear α-Mn_2O_3 (221) peaks and the shrinking of NiO (222) peak from $x = 1.0$ until it disappears at $x = 0.4$.

B. Solid solution of $Ni_kMn_{1-k}O$

In this compositional range $0.9 < x \le 1$, a solid solution is formed whose composition can be tuned. The resulting solid solution has the rock-salt phase (space group: $Fm\bar{3}m$). The XRD data in Fig. 1(a) show pure phases for NiO and α-Mn_2O_3 cubic phases and Fig. 1(b) shows the (200) peak of the rock-salt phase (at 43.3°) for $Ni_kMn_{1-k}O$ solid solutions. The 43.3° peak position shifts monotonically to lower angles with the increase of manganese concentration. Figure 1(c) shows the plot of the variation of lattice parameter with Mn mol% doping in Ni lattice. Clearly, the lattice parameter increases non-linearly until it reaches the solubility limit which is about 10 mol% Mn composition or $x = 0.90$. It is noteworthy that at compositions above the solubility limit of Mn in Ni lattice, the speciation of the spinel phase is more evident. The crystal structure of sample with $x = 0.90$ was examined with HRTEM and the SAED, and the result is in agreement with the XRD results (Fig. 2).

https://doi.org/10.1557/jmr.2016.92 Published online by Cambridge University Press

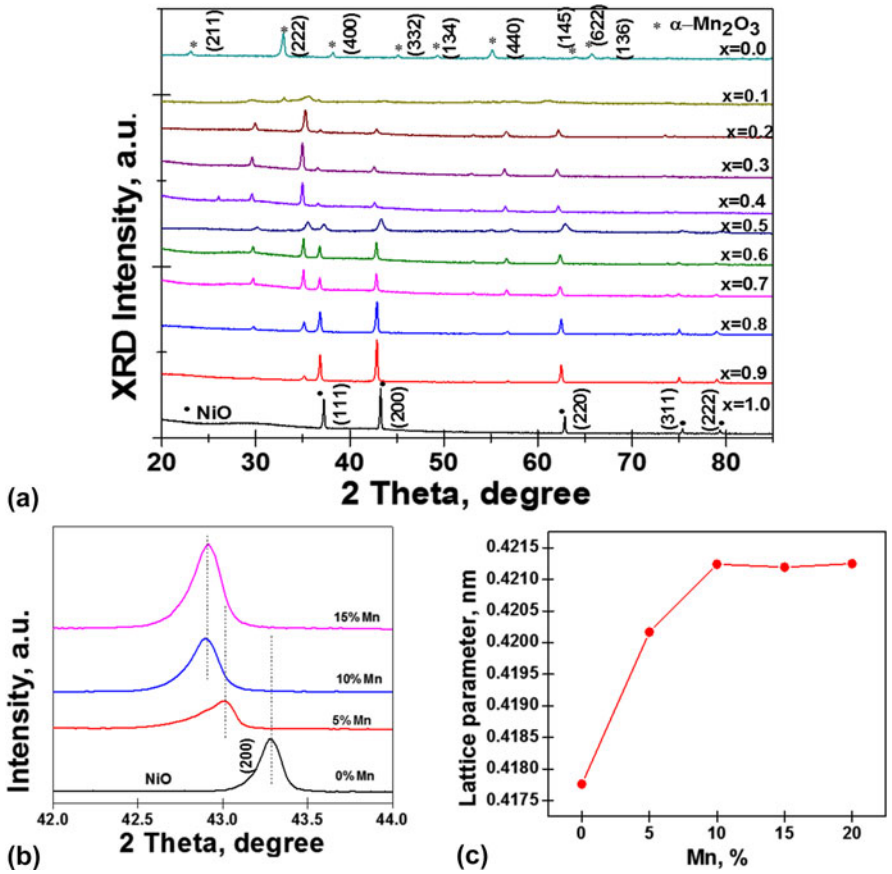


FIG. 1. (a) XRD of $Ni_xMn_{1-x}O_y$ ($0.0 \leq x \leq 1.0$) showing the phases present as x is varied, 2 theta range of 42–44°marked by (200) peak is expanded in (b) for clarity. (b) XRD showing the (200) plane of NiO lattice shifting to a lower angle with Mn doping. (c) Variation of the NiO lattice parameter with Mn doping concentration.

C. Solid solution of $Ni_mMn_{3-m}O_4$ spinel

In this compositional range $0.05 < x \leq 0.9$, the XRD data for samples were indexed to spinel solid solutions ($Ni_mMn_{3-m}O_4$). The sample with composition $x = 0.30$ showed well-resolved diffraction lines corresponding to a tetragonal spinel phase (ICDD PDF-01-070-9039) with space group number $I4_1/amd$ (141). XRD data for samples with the following x composition and the corresponding m values in bracket: 0.50 (1.50), 0.40 (1.20), 0.30 (0.90), 0.25 (0.75), 0.20 (0.60), show that phase pure $Ni_mMn_{3-m}O_4$ bimetal spinel solid solutions exist in the composition range $0.20 < x \leq 0.50$ (or $0.60 < m \leq 1.50$). The series of oxides with composition $0.05 < x \leq 0.20$ shows peak deviation from nickel manganite peaks, and peaks at (112) and (103) were highlighted in Fig. S2 (Supplementary information) for emphasis. There is a widening of the gap between the centerlines of these two peaks coupled with peak broadening until manganese oxide (Mn_3O_4 and α-Mn_2O_3) peaks are evolved at $x = 0.05$. Peak broadening can be ascribed to the non-uniform strain on the spinel lattice. It is interesting to note that at nickel composition $x \leq 0.05$, there is not enough Ni(II) to diffuse into the solid lattice of Mn_3O_4 to occupy the manganese vacancies or partially replace manganese ions in the tetrahedral or octahedral holes.[28] In the compositional range $0.5 < x \leq 0.9$, there is a co-existence of spinel solid solutions and rock-salt ($Ni_{0.9}Mn_{0.1}O$), however; at $x > 0.5$, only phase pure $Ni_mMn_{3-m}O_4$ can be seen. Similar bimetallic oxide systems were reproduced for the nickel ferrite, available in the Supplementary information Fig. S3.

The spinel manganites are known to exhibit large tetragonal distortions.[29,30] The tetragonal distortion is a consequence of Jahn–Teller effect of the cubic spinel associated with a high density of Mn^{3+} cations.[31] Large amounts of Mn^{3+} are found in Mn-rich nickel–manganese spinels due to the reduced amount of Ni^{2+} on the octahedral sites of the spinel lattice.[32] The Mn valence states are strongly dependent on Ni occupancy in the octahedral sublattice, which is a measure of inversion parameter of the spinel lattice. Ni cations moving to the octahedral sublattice are balanced by the Mn going in the opposite way (tetrahedral sites). The tetrahedral Mn has a valence state of +2 since Mn^{3+} is a less suitable state in a 4-fold

https://doi.org/10.1557/jmr.2016.92 Published online by Cambridge University Press

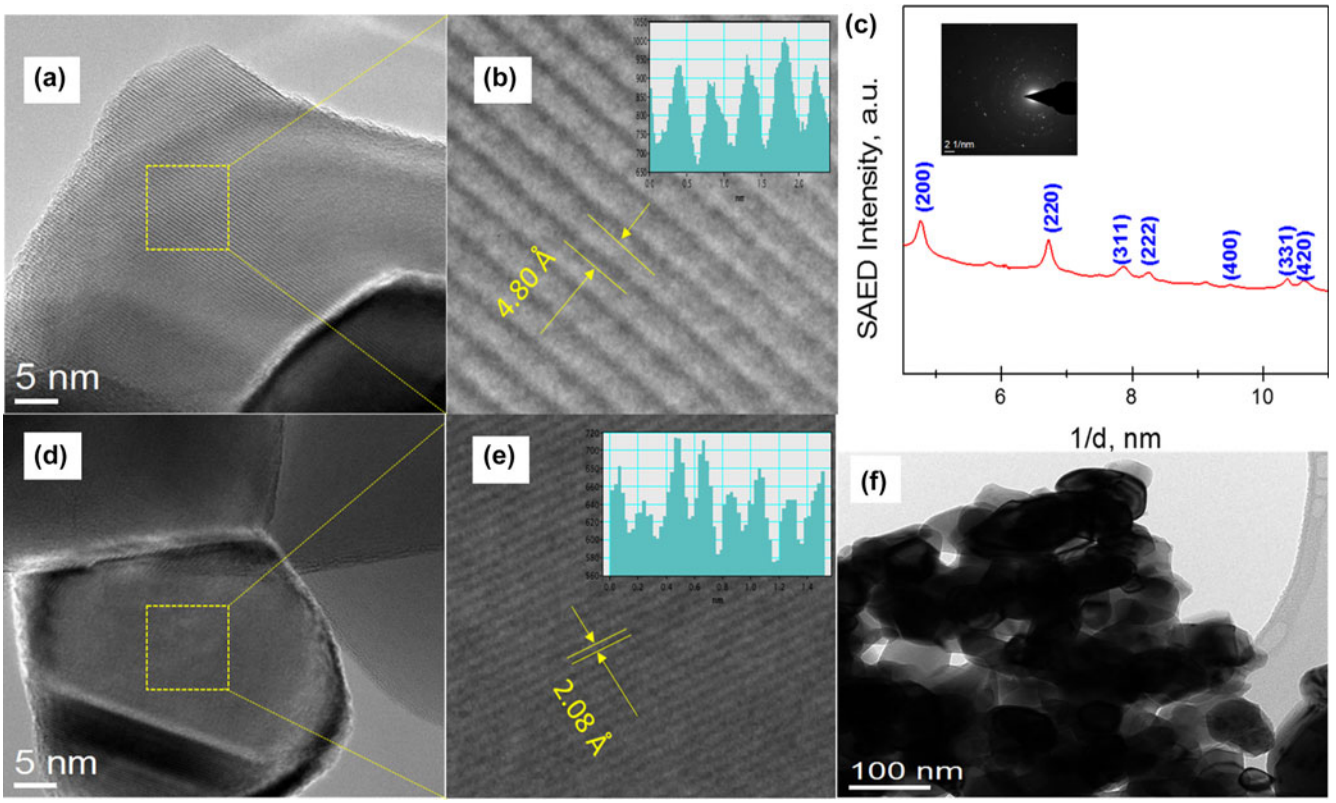


FIG. 2. (a) HR-TEM of sample $x = 0.9$, showing grains with single lattice fringes having d-spacing indexed to (101) of the tetragonal spinel lattice, (b) a close-up view of the lattice fringes showing d_{101} to be 4.80 Å, (c) SAED of sample $x = 0.9$ (inset) showing the diffraction rings. The intensity line profiles measured from these patterns are as shown, assigned to the rocksalt phase with some spinel peaks, which is in agreement with XRD data, (d) HR-TEM of sample $x = 0.9$, showing grains with single lattice fringes having d-spacing indexed to (200) of the rocksalt lattice, (e) a close-up view of the lattice fringes showing d_{200} to be 2.08 Å, and (f) bright field TEM of composition $x = 0.9$.

coordination. To attain charge neutrality, an equal amount of Mn^{4+} is formed in the octahedral sites to compensate for the Mn^{2+} on the tetrahedral sites, resulting into internal disproportionation.[33]

The XRD data are further corroborated with diffraction and EDX analysis using HRTEM. A representative sample $x = 0.2$ is used as an example to confirm the morphology and crystal structure. Figure 3(a) shows the bright field TEM image for the solid solution with composition $x = 0.2$ where a rapidly changing strong diffraction contrast can be noticed, an indication of randomly oriented grains and polycrystallinity of sample. The SAED patterns obtained for sample $x = 0.2$ are shown in the inset of Fig. 3(b). The intensity line profiles measured from these patterns are shown in Fig. 3(b). About ten diffraction rings are visible which correspond to the family of planes of the tetragonal spinel nickel manganite; the other rings were not clearly detectable due to their low intensity. Formation of tetragonal spinel phase is further confirmed from the sample with composition $x = 0.2$ by the HRTEM analysis. We identified two of lattice fringes, one with the d-spacing of 4.85 Å and the other one with the d-spacing of 3.00 Å, which are consistently observed in HRTEM images of the nanoparticles [Fig. 3(c)]. Knowing that the typical accuracy of HRTEM analysis is usually not better than a few percent, the observed lattice fringes can be assigned to the (101) and (200) planes of tetragonal spinel $Ni_{0.6}Mn_{2.4}O_4$. As expected, the HRTEM data did not show any presence of α-Mn_2O_3 and NiO phases in this sample composition. SEM image [Fig. 3(d)] of the solid solution with sample composition $x = 0.2$ has a morphology resembling cubes interconnected by a channel. Figure 4 shows TEM-EDX compositions of four randomly selected grains of samples with precursor compositions $x = 0.1$ to $x = 0.9$, showing strong agreement with the precursor composition.

D. Comparison between plasma and thermal oxidation

To understand whether one can obtain similar results with thermal oxidation, a sample with composition $x = 0.2$ is investigated using thermal oxidation route. The phases obtained were the ilmenite ($NiMnO_3$), bixbyite (α-Mn_2O_3), and the bunsenite (NiO) phases, which are completely different from the result obtained with plasma oxidation (refer to Fig. 5). The difference in the phases can be ascribed to the dissimilar mechanistic steps obtainable

https://doi.org/10.1557/jmr.2016.92 Published online by Cambridge University Press

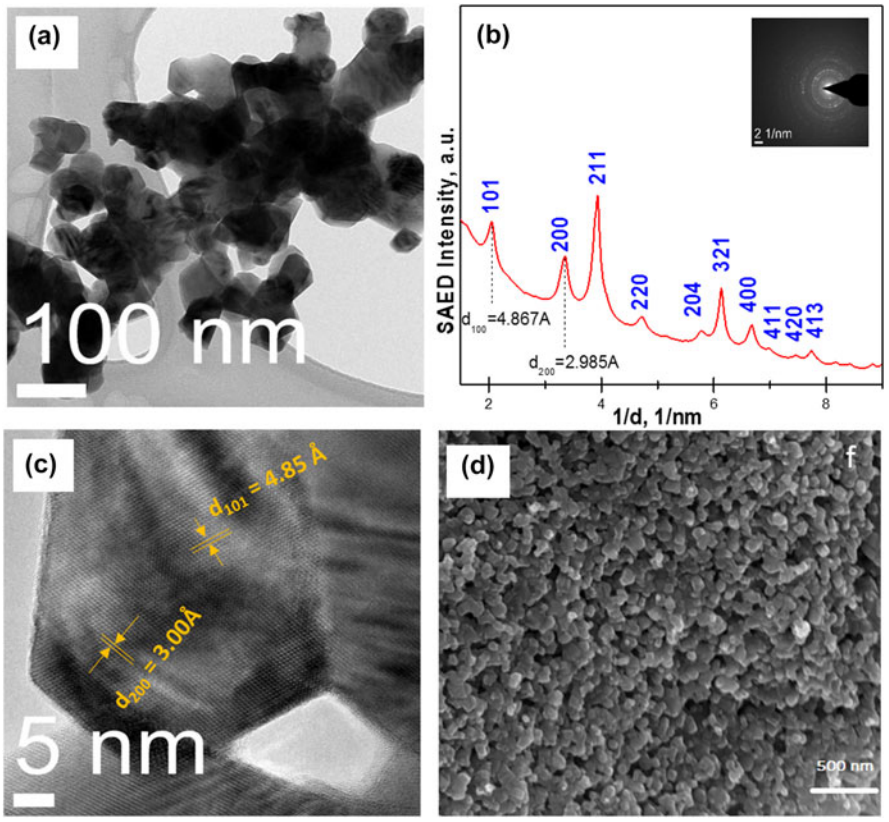


FIG. 3. (a) Bright field TEM of composition $x = 0.2$ with a crystallite size of 50–80 nm, (b) SAED of sample $x = 0.2$ (inset) showing ten diffraction rings. The intensity line profiles measured from these patterns are as shown, assigned to the tetragonal spinel, which is in agreement with XRD data, (c) HR-TEM showing grains with two lattice fringes having *d*-spacing indexed to (101) and (200) planes of the tetragonal spinel crystals, and (d) SEM micrograph of samples $x = 0.2$ showing its morphology.

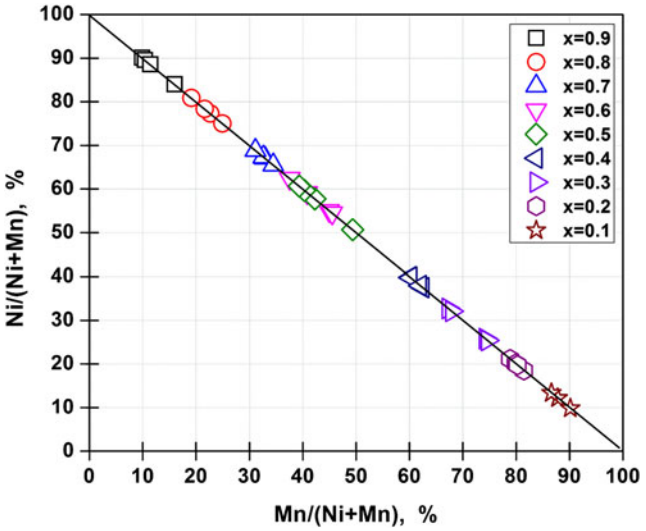


FIG. 4. TEM-EDX composition of the four selected nanoparticle grains with Ni at.% on the vertical axis and Mn at.% on the horizontal axis.

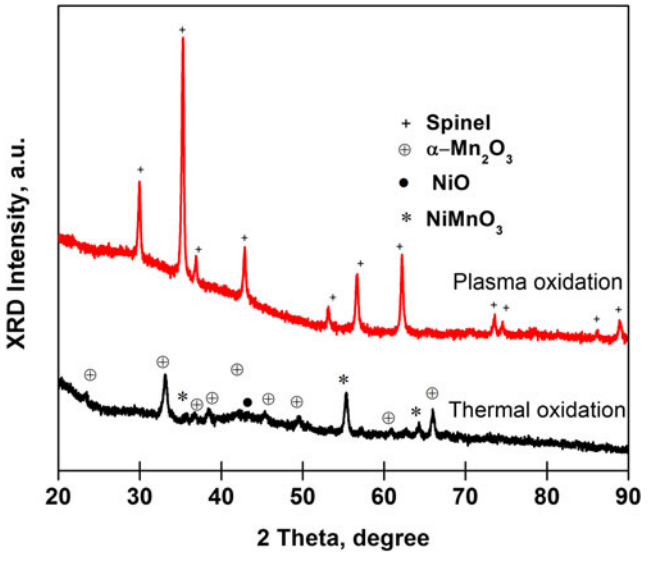


FIG. 5. X-ray diffraction of the sample with nominal composition of x=0.2 prepared via plasma and thermal oxidation.

in the two oxidation processes, given that the reaction temperature and pressure are same. As can be seen from the results, plasma oxidation better reflects the reaction off-stoichiometry, producing solid solution of nickel manganite spinel. However, the thermally oxidized sample are segregated into thermodynamically stable monometal

https://doi.org/10.1557/jmr.2016.92 Published online by Cambridge University Press

oxide (bunsenite and bixbyite) and mixed metal oxide (ilmenite) phases in agreement with Xiao-Xia and co-workers.[34]

To explain the differences between thermal and plasma oxidation, a proposed mechanism as elucidated by the schematic presented in Fig. 6 is used to illustrate various stages of oxidation process. The following are the stages of oxidation: first of all, upon either plasma exposure or thermal heating, the liquid droplet will lose solvent by evaporation until a densified amorphous phase is formed. In the case of thermal oxidation, heating and cooling rates are slow and so atoms have enough time to diffuse, inducing a phase transformation toward thermodynamically stable phases. So, irrespective of precursor composition inside liquid droplets, the resulting materials would consist of thermodynamically stable phases. The oxidation proceeds with diffusion of molecular oxygen into the amorphous mass containing nitrates and the thermal decomposition of the amorphous mass to release NO_x. After an induction period, nuclei are formed. In the case of plasma oxidation, several processes take place in a very short period of time of a few seconds and they include the following: oxygen radicals can diffuse into the core of the densified amorphous mass of precursor; faster reaction kinetics with oxidation of nitrates with oxygen radicals; and fast heating and cooling rates of the core for nucleation and transport limited ordering of atoms make for the speciation of metastable phase nuclei. As the growth proceeds with transport limited region, the composition of resulting solid solutions depends directly on the composition of elements in the surrounding environment. The composition of the surrounding nutrients is as homogenous and similar to the supersaturation; thus, the growing crystals reflect this compositional homogeneity and on rapid cooling, the diffusion of atoms is suppressed, which leads to a non-equilibrium solid solution phase growth. Average size of crystallites obtained in plasma oxidation is about twice that of thermal oxidation indicating fast growth kinetics compared to thermal oxidation.

E. Ternary solid solutions of $NiMn_zFe_{2-z}O_4$ ($0 \leq z \leq 1$)

Ternary spinel oxides comprising manganese substituted nickel ferrite, with nominal series formula $NiMn_zFe_{2-z}O_4$ (where z = 0.0, 0.20, 0.40, 0.60, 0.80, and 1.0) have been successfully synthesized by the plasma spray method. The XRD reflections [Fig. 7(a)] show highly crystalline nanoparticles with exceptional phase purity. Figure 7(b) shows an expanded view of (311) peak position. As can be seen, there is a monotonic

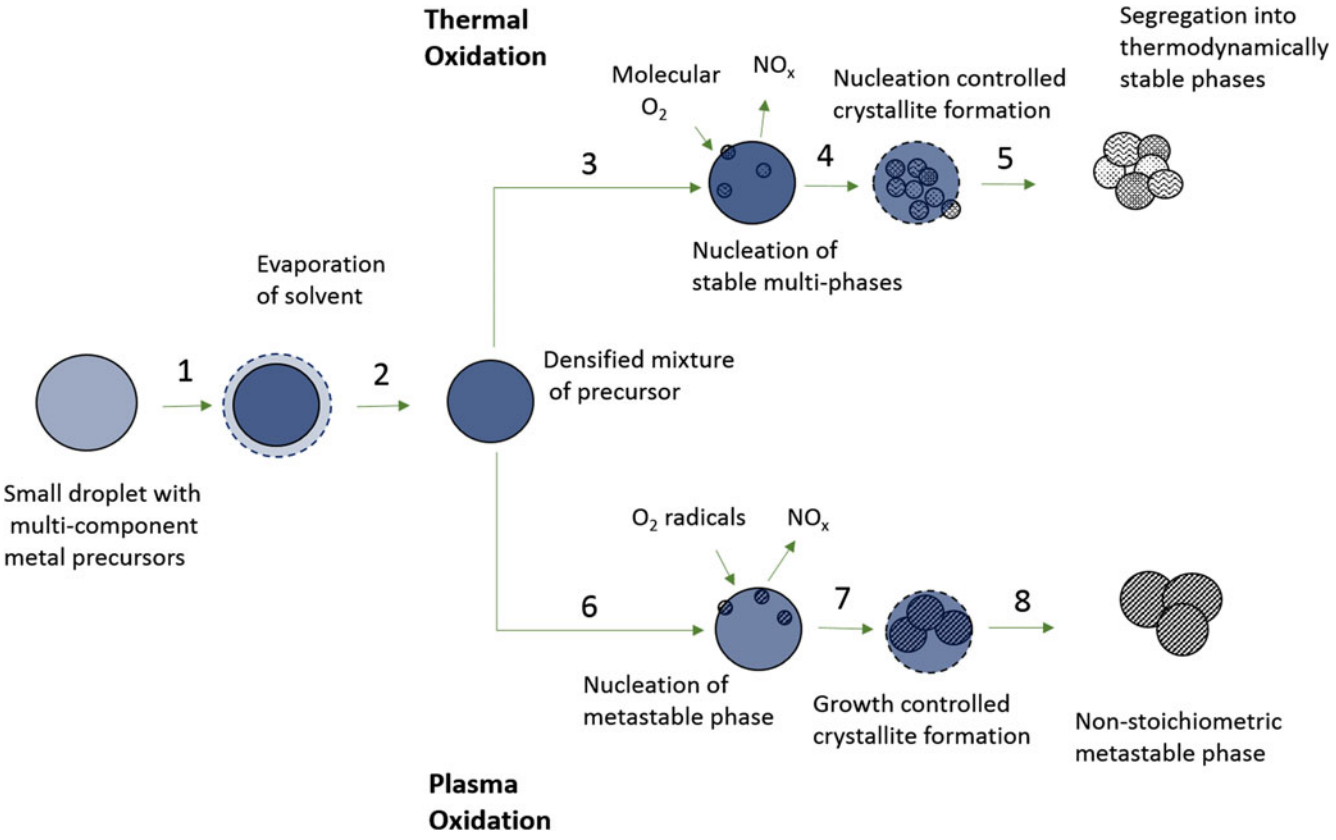


FIG. 6. Proposed mechanism for the formation of nanoparticles of thermally oxidized and plasma oxidized precursor solutions.

https://doi.org/10.1557/jmr.2016.92 Published online by Cambridge University Press

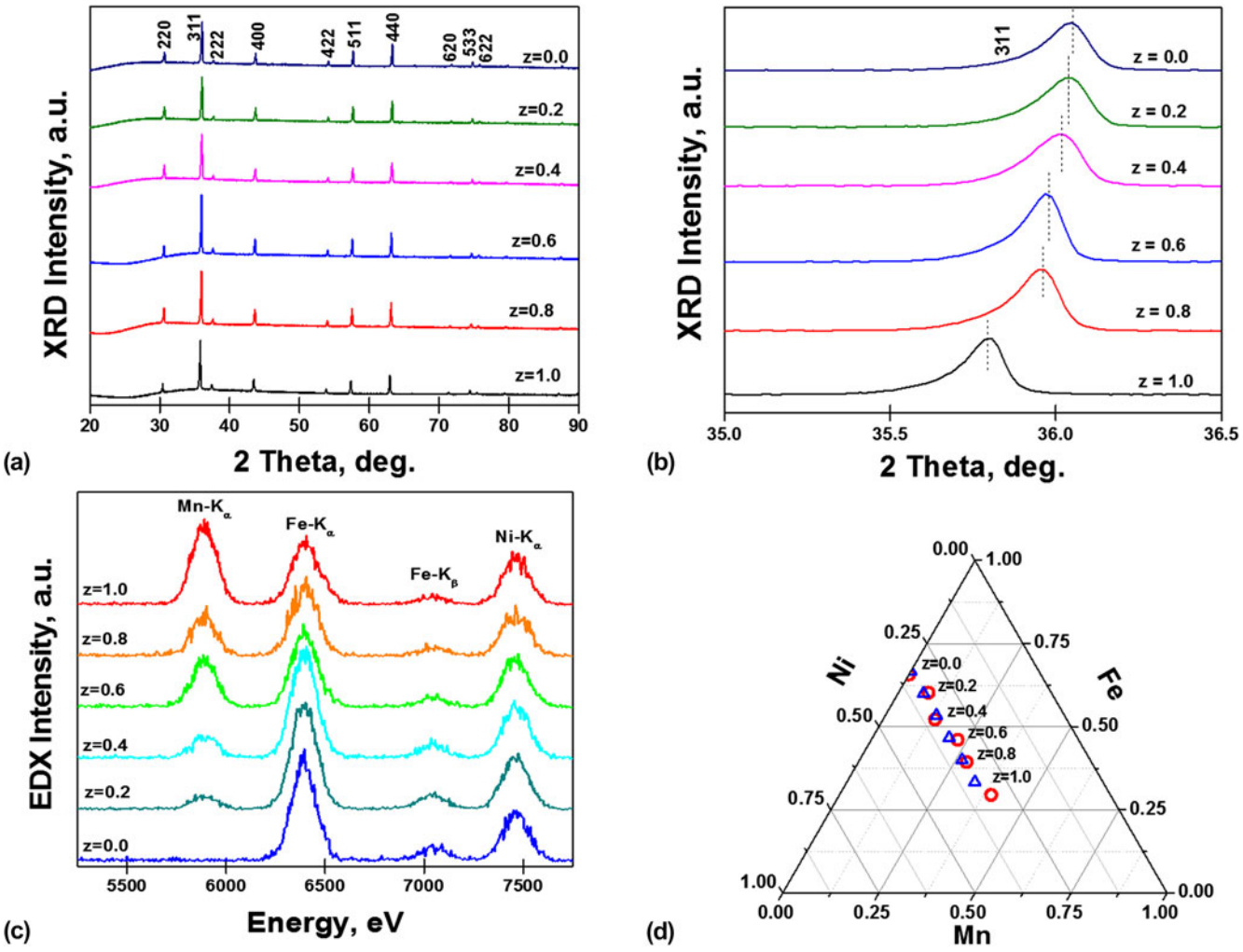


FIG. 7. (a) XRD reflections of ternary spinel oxides comprising manganese substituted nickel ferrite $NiMn_zFe_{2-z}O_4$ ($0 \leq z \leq 1$) showing a single cubic spinel phase. (b) Zoom-in of (311) peak position showing a monotonic shift to a lower angle with increasing Mn doping concentration. (c) TEM-EDX spectra obtained at 0–20 kV, along with peak assignments for Mn, Ni, and Fe elements for various compositions ($0 \leq z \leq 1$). (d) Ternary plot of $NiMn_zFe_{2-z}O_4$ ($0 \leq z \leq 1$) showing an excellent match between the nominal precursor composition (Δ) and the TEM-EDX measured alloy composition (○), in normalized atomic percent.

shift of the 311 peak position to the left with increasing manganese doping, an indication of the formation of a spinel solid solution. The same family of peaks indexed to cubic spinel phase (space group: $Fm\bar{3}m$) appears in all six samples and no foreign peak was observed, an indication that no other phase co-existed with sample phase. The domain size of microstrain was estimated from Williamson–Hill (W–H) plots (Supplementary information S4) and tabulated as shown in Table I. After a linear fit to the W–H plot, the microstrain and domain size were extracted from the slope and vertical axis intercept, respectively. Results reveal that the strain portion of the W–H plot has no contribution to the line broadening (Supplementary Fig. S4) except for the sample $z = 1.0$ with negligible microstrain (0.01%) as shown by Table I. The lattice parameter and unit cell volume expand isotropically as the density of the manganese dopant increases, and the crystal size is in the range 500–590 Å. For uniform strain, the unit cell dimensions change in an isotropic manner which leads to changes of the lattice parameters and a shift of the peaks with no accompanying broadening of the XRD

TABLE I. Structural parameters of $NiMn_zFe_{2-z}O_4$ ($0.0 \leq z \leq 1.0$) showing how lattice parameter, unit cell volume and anisotropic strain vary υ composition.

z	Lattice parameter (Å)	Cell volume (Å^3)	Domain size (Å)	Strain (%)
0.0	8.3347	579.0	590.5	...
0.2	8.3369	579.4	505.6	...
0.4	8.3415	580.4	500.7	...
0.6	8.3528	582.8	587.1	...
0.8	8.3573	583.7	521.5	...
1.0	8.3938	591.4	574.4	0.01

https://doi.org/10.1557/jmr.2016.92 Published online by Cambridge University Press

reflections. The shape of peaks are unchanged from $z = 0.0$ to $z = 1.0$ which confirms the absence of anisotropic microstrain.

Figure 7(c) shows the typical EDX spectra obtained at 0–20 kV, along with peak assignments for Mn, Ni, and Fe elements for various compositions ($0 \leq z \leq 1$). The peak areas fairly match the precursor compositions, confirming the formation of ternary solid solutions [Fig. 7(d)]. After integrating the peak areas of Mn–K_α, Ni–K_α, Fe–K_α, and Fe–K_β, we converted the x-ray counts into the elemental weight percentages using quantification software. The elemental analysis of the nanoparticles confirms that the proportion of the elements is consistent with the precursor composition (Table II). Figure 8 shows the XRD patterns and corresponding Rietveld analysis of as-prepared sample $NiMn_{0.2}Fe_{1.8}O_4$, confirming the formation of spinel phases. Rietveld refinement and Bertaut method[35] are used to determine the cation distribution (Supplementary information, Table S1). Combining the refined results and TEM elemental analysis, the structural formula of $NiMn_{0.2}Fe_{1.8}O_4$ was determined to be $(Ni_{0.1}Mn_{0.15}Fe_{0.75})_{8a}[Ni_{0.9}Mn_{0.05}Fe_{1.05}]_{16d}O_4$, revealing a high degree of inversion in agreement with other results for ferrite spinel,[36] where the parenthesis refers to the tetragonal sites while octahedral sites are represented by square brackets. For an AB_2O_4 type spinel, the extent to which sublattices are disordered is determined by the inversion parameter i which is the fraction of B^{3+} occupying the tetragonal sites, as such i can vary from 0, which corresponds to normal spinel and 1, which refers to a structure where all the tetragonal sites are occupied by B^{3+}.

TABLE II. TEM-EDX analyzed composition of $NiMn_zFe_{2-z}O_4$ ($0.0 \leq z \leq 1.0$).

	TEM-EDX analyzed composition, at.%			
z	O	Mn	Fe	Ni
0.0	61.9 ± 0.7	...	25.1 ± 0.6	13.1 ± 0.5
0.2	61.8 ± 0.4	3.1 ± 0.1	23.6 ± 0.4	12.5 ± 0.3
0.4	61.0 ± 0.4	5.3 ± 0.2	20.4 ± 0.3	13.4 ± 0.3
0.6	58.2 ± 0.5	9.4 ± 0.3	19.3 ± 0.4	13.1 ± 0.4
0.8	57.4 ± 0.4	12.0 ± 0.3	16.8 ± 0.3	13.8 ± 0.3
1.0	55.5 ± 0.5	17.6 ± 0.4	13.1 ± 0.3	13.8 ± 0.3

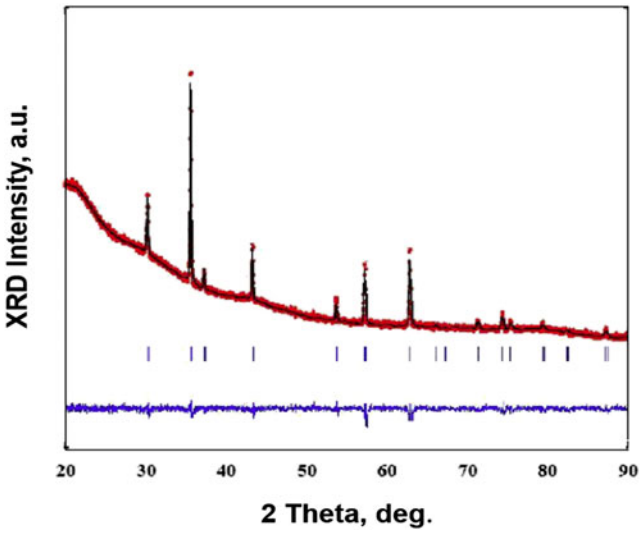


FIG. 8. Structural analysis of the synthesized nanocrystalline spinels $NiMn_{0.2}Fe_{1.8}O_4$ showing Rietveld refined XRD patterns with experimental data (black line), calculated profiles (red dots), allowed Bragg diffraction positions (vertical bars) and difference curve (blue line).

F. OER kinetics

A series of $NiMn_zFe_{2-z}O_4$ ($z = 0$, 0.20, 0.40, 0.60, 0.80 and 1.0) mixed metal oxide films were tested for OER catalysis by studying the cyclic voltammetry at 20 mV/s scan rate. Two parameters were selected to understand the catalyst performance: (i) overpotential (η) required to reach a current density of 10 mA/cm^2; (ii) steady state Tafel slope (mV/decade).

The data in Fig. 9(a) show a decrease in η for OER catalysts with increase in Mn content in the binary metal oxide nickel ferrite. Pure nickel ferrite shows higher overpotential of 0.46 V compared to the ternary metal oxides. Among all the six compositions, $z = 0.20$ demonstrates the lowest η at 0.39 V. There still remains the challenge of impartially comparing the efficiencies of electrocatalysts, largely due to complications arising from both inadequate standardizations and deviations in average particle size and/or surface areas. It is also notable that the manganese doped ternary metal oxides are more active catalysts than stand-alone NiO_x, FeO_x, or MnO_x catalysts. The NiO_x-type catalyst has been previously reported to give 10 mA/cm^2 at an overpotential value of ~0.42 V,[37,38] and the reported overpotential value at a current density of 1.0 mA/cm^2 for FeO_x and MnO_x based catalyst are 0.41 and 0.51 V, respectively,[39] which are expected to be at a higher overpotential value when adjusted to the benchmarking current density of 10 mA/cm^2. Substitution of cations into complex metal oxide crystal lattice has been known to induce oxygen vacancies, and according to Bao et al.,[40] there is a positive correlation between oxygen vacancy and electrocatalytic activity in OER of nickel-cobalt oxide based catalysts, of which they adduced low H_2O adsorption energy at the defect site to this outcome.

The linear part of the Tafel plots is shown in Fig. 9(b) obtained for all the six compositions in the overpotential window of $\eta = 0.35$–0.50 V. The electrodes with lower z value shows smaller Tafel slopes less than 45 mV/decade compared to the electrodes with higher content of Mn doping indicating an improvement in the electrocatalytic activity of the catalyst. The data presented in Table III

https://doi.org/10.1557/jmr.2016.92 Published online by Cambridge University Press

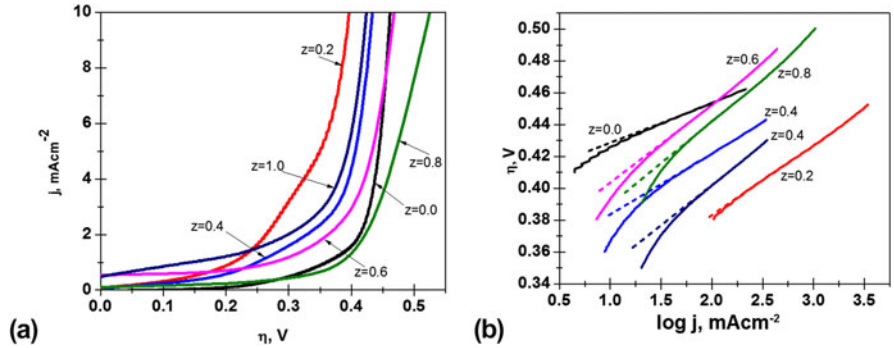


FIG. 9. (a) Cyclic voltammetry of the conditioned $NiMn_zFe_{2-z}O_4$ ($0 \leq z \leq 1$) films collected in 1 M NaOH solution at a scan rate of 20 mV s^{-1}; (b) Steady state Tafel plot for the linear region from 0.35 – 0.50 V.

TABLE III. Electrode kinetic parameters for the OER of $NiMn_zFe_{2-z}O_4$ ($0.0 \leq z \leq 1.0$) in 1 M NaOH at 298 K.

z	η, V @ 10 mA/cm^2	Tafel slope (0.35–0.50 V), mV/dec
0.0	0.46	44.9
0.2	0.39	42.7
0.4	0.43	38.8
0.6	0.46	61.2
0.8	0.45	76.6
1.0	0.42	60.2

show the variation of the overpotential and linear portion of the Tafel slope with composition. The values of the Tafel slope found on the manganese substituted nickel ferrite solid solutions are comparable to those found elsewhere: $MnFe_{2-x}Cr_xO_4$ (~40 mV/decade)[41] and $NiFe_{2-x}Cr_xO_4$ (~40 mV/decade).[42] Strasser and co-workers[43] found through experimental and first principle studies that compressive strain in Pt–Cu solid solution have a strong correlation with its electroactivity in oxygen reduction reaction. Also, the improved activity of the alloy may have been due to the favorable adjustment of the electronic properties of the alloy as a direct effect of the combination of the completely filled *d* orbitals (Ni) with semifilled orbitals (Mn and Fe) according to the Brewer–Engel theory.[44]

Besides high catalytic activity, an optimal catalyst material should be stable for their implementation in any operating system. The stability of these catalysts under catalytic conditions was determined using controlled-current electrolysis. The catalyst material was held at a constant current density of 10 mA/cm^2 per geometric area for 2 h, while the operating potential was measured as a function of time. Figure S5 from the Supplementary information shows the results of the controlled current electrolysis measurements of these catalysts. Clearly, η (t = 0) and η (t = 2 h) are similar, an indication that the catalyst is stable under the operating conditions for at least a 2 h period.

The concept of plasma oxidation of precursor solution mentioned here offers excellent metastable phase formation possibilities due to its fast reaction kinetics and cooling rates. In general, short reaction times allow for the formation of either transient phases in the case of monometal oxides or solid solutions in the case of mixed metal oxides.[45] The process is highly adaptable to any precursor chemical (inorganic, organic, etc.) and any solvent (aqueous, polar, nonpolar, organic, etc.) which can be easily incorporated into the spray feedstock. Precursor solution mixtures can be used to produce multicomponent systems such as bimetallic and ternary oxides and their solid solutions. Since each droplet contains precursor chemicals in the same stoichiometric composition as desired in the produced particle, the synthesized particles will have exceptional compositional uniformity.

IV. CONCLUSIONS

We have successfully demonstrated a synthesis technique based on plasma oxidation of liquid droplets for producing mixed metal oxide solid solutions with controllable composition over entire range. Specific experiments were presented with binary and ternary metal oxides involving nickel, manganese and iron as elements. The selective formation of rocksalt and spinel solid solution is a direct consequence of the precise compositional control shown in this method and will be very useful in tuning catalytic properties in many process applications. As an example, we have demonstrated rapid screening of several mixed metal oxide solid solution systems by testing a series of manganese substituted nickel ferrite materials for their activity with OER reaction in alkaline media. The results showed that the presence of a small amount of manganese (z = 0.20) caused a significant drop in the overpotential with excellent Tafel kinetics.

ACKNOWLEDGMENTS

The authors acknowledge primary funding support from NSF Solar Project (DMS 1125909) and access to facilities at the Conn Center for Renewable Energy

https://doi.org/10.1557/jmr.2016.92 Published online by Cambridge University Press

Research. This material is partially based upon work supported by the National Science Foundation under Cooperative Agreement No. 1355438. The first and third authors thank the University of Louisville for funding through the Ph.D. fellowship award. We thank Dr. S.E. Shirsath for his assistance with Rietveld refinement analysis.

REFERENCES

1. P. Yang and J-M. Tarascon: Towards systems materials engineering. *Nat. Mater.* **11**, 560–563 (2012).
2. N.S. Lewis and D.G. Nocera: Powering the planet: Chemical challenges in solar energy utilization. *Proc. Natl. Acad. Sci. U. S. A.* **103**, 15729–15735 (2006). doi: 10.1073/pnas.0603395103.
3. F. Cheng, J. Shen, B. Peng, Y. Pan, Z. Tao, and J. Chen: Rapid room-temperature synthesis of nanocrystalline spinels as oxygen reduction and evolution electrocatalysts. *Nat. Chem.* **3**, 79–84 (2011). (http://www.nature.com/nchem/journal/v3/n1/abs/nchem.931.html#supplementary-information).
4. D.V. Yandulov and R.R. Schrock: Catalytic reduction of dinitrogen to ammonia at a single molybdenum center. *Science* **301**, 76–78 (2003). doi: 10.1126/science.1085326.
5. J. Armijo: The kinetics and mechanism of solid-state spinel formation—A review and critique. *Oxid. Met.* **1**, 171–198 (1969).
6. A. Stein, S.W. Keller, and T.E. Mallouk: Turning down the heat: Design and mechanism in solid-state synthesis. *Science* **259**, 1558–1564 (1993).
7. K.K. Banger, Y. Yamashita, K. Mori, R.L. Peterson, T. Leedham, J. Rickard, and H. Sirringhaus: Low-temperature, high-performance solution-processed metal oxide thin-film transistors formed by a 'sol–gel on chip' process. *Nat. Mater.* **10**, 45–50 (2011). (http://www.nature.com/nmat/journal/v10/n1/abs/nmat2914.html#supplementary-information).
8. R.M. Rojas, E. Vila, O. García, and J.L.M. de Vidales: Thermal behaviour and reactivity of manganese cobaltites $Mn_xCo_{3-x}O_4$($0.0 \leq x \leq 1.0$) obtained at low temperature. *J. Mater. Chem.* **4**, 1635–1639 (1994).
9. Y. Matsushita, H. Ueda, and Y. Ueda: Flux crystal growth and thermal stabilities of LiV_2O_4. *Nat. Mater.* **4**, 845–850 (2005).
10. D. Seley, K. Ayers, and B. Parkinson: Combinatorial search for improved metal oxide oxygen evolution electrocatalysts in acidic electrolytes. *ACS Comb. Sci.* **15**, 82–89 (2013).
11. J.A. Bau, P. Li, A.J. Marenco, S. Trudel, B.C. Olsen, E.J. Luber, and J.M. Buriak: Nickel/iron oxide nanocrystals with a nonequilibrium phase: Controlling size, shape, and composition. *Chem. Mater.* **26**, 4796–4804 (2014). doi: 10.1021/cm501881a.
12. S.E. Pratsinis: Flame aerosol synthesis of ceramic powders. *Prog. Energy Combust. Sci.* **24**, 197–219 (1998). doi: 10.1016/S0360-1285(97)00028-2.
13. G.L. Messing, S.C. Zhang, and G.V. Jayanthi: Ceramic powder synthesis by spray pyrolysis. *J. Am. Ceram. Soc.* **76**, 2707–2726 (1993).
14. D.J. Lewis: Technique for producing mullite and other mixed-oxide systems. *J. Am. Ceram. Soc.* **74**, 2410–2413 (1991).
15. B. Marshall, I. Telford, and R. Wood: A field method for the determination of zinc oxide fume in air. *Analyst* **96**, 569–578 (1971).
16. R. Mueller, R. Jossen, S.E. Pratsinis, M. Watson, and M.K. Akhtar: Zirconia nanoparticles made in spray flames at high production rates. *J. Am. Ceram. Soc.* **87**, 197–202 (2004).
17. J.E. Katz, T.R. Gingrich, E.A. Santori, and N.S. Lewis: Combinatorial synthesis and high-throughput photopotential and photocurrent screening of mixed-metal oxides for photoelectrochemical water splitting. *Energy Environ. Sci.* **2**, 103–112 (2009). doi: 10.1039/B812177J.
18. V. Kumar, J.H. Kim, C. Pendyala, B. Chernomordik, and M.K. Sunkara: Gas-phase, bulk production of metal oxide nanowires and nanoparticles using a microwave plasma jet reactor. *J. Phys. Chem. C* **112**, 17750–17754 (2008). doi: 10.1021/jp8078315.
19. M. Hasegawa, Y. Kato, M. Kagawa, and Y. Syono: Effect of additive oxides on ultrafine CeO_2 particles synthesized by the spray-ICP technique. *J. Mater. Sci. Lett.* **15**, 1608–1611 (1996).
20. M. Suzuki, M. Kagawa, Y. Syono, and T. Hirai: Synthesis of ultrafine single-component oxide particles by the spray-ICP technique. *J. Mater. Sci.* **27**, 679–684 (1992).
21. M. Schaefer, A. Kumar, R. Mohan Sankaran, and R. Schlaf: Synthesis and in vacuo deposition of iron oxide nanoparticles by microplasma-assisted decomposition of ferrocene. *J. Appl. Phys.* **116**, 133703 (2014). doi: 10.1063/1.4897165.
22. M. Marr, J. Kuhn, C. Metcalfe, J. Harris, and O. Kesler: Electrochemical performance of solid oxide fuel cells having electrolytes made by suspension and solution precursor plasma spraying. *J. Power Sources* **245**, 398–405 (2014).
23. S.M. Chang, R. Tolava, F. Erwin, Y.J. Yang, H.C. Li, R.C. Lee, N.L. Wu, and C.C. Hsu: One-step fast synthesis of $Li_4Ti_5O_{12}$ particles using an atmospheric pressure plasma jet. *J. Am. Ceram. Soc.* **97**, 708–712 (2014).
24. T.R. Cook, D.K. Dogutan, S.Y. Reece, Y. Surendranath, T.S. Teets, and D.G. Nocera: Solar energy supply and storage for the legacy and nonlegacy worlds. *Chem. Rev.* **110**, 6474–6502 (2010). doi: 10.1021/cr100246c.
25. J. Suntivich, K.J. May, H.A. Gasteiger, J.B. Goodenough, and Y. Shao-Horn: A Perovskite oxide optimized for oxygen evolution catalysis from molecular orbital principles. *Science* **334**, 1383–1385 (2011). doi: 10.1126/science.1212858.
26. J.B. Gerken, J.Y.C. Chen, R.C. Massé, A.B. Powell, and S. S. Stahl: Development of an O_2-sensitive fluorescence-quenching assay for the combinatorial discovery of electrocatalysts for water oxidation. *Angew. Chem., Int. Ed.* **51**, 6676–6680 (2012). doi: 10.1002/anie.201201999.
27. C. Xiang, S.K. Suram, J.A. Haber, D.W. Guevarra, E. Soedarmadji, J. Jin, and J.M. Gregoire: High-throughput bubble screening method for combinatorial discovery of electrocatalysts for water splitting. *ACS Comb. Sci.* **16**, 47–52 (2014). doi: 10.1021/co400151h.
28. R.G. Burns: The uptake of cobalt into ferromanganese nodules, soils, and synthetic manganese (IV) oxides. *Geochim. Cosmochim. Acta* **40**, 95–102 (1976). doi: 10.1016/0016-7037(76)90197-6.
29. S.W. Ko, J. Li, N.J. Podraza, E.C. Dickey, and S. Trolier-McKinstry: Spin spray-deposited nickel manganite thermistor films for microbolometer applications. *J. Am. Ceram. Soc.* **94**, 516–523 (2011). doi: 10.1111/j.1551-2916.2010.04097.x.
30. H-J. Noh, S. Yeo, J-S. Kang, C.L. Zhang, S-W. Cheong, S-J. Oh, and P.D. Johnson: Jahn-Teller effect in spinel manganites probed by soft x-ray absorption spectroscopy. *Appl. Phys. Lett.* **88**, 081911 (2006). doi: 10.1063/1.2178474.
31. S. Miyahara: Jahn-Teller distortion in magnetic spinels. *J. Phys. Soc. Jpn.* **17**, 181–184 (1962).
32. G. de Györgyfalva and I. Reaney: Decomposition of $NiMn_2O_4$ spinels. *J. Mater. Res.* **18**, 1301–1308 (2003).
33. A. Díez, R. Schmidt, A.E. Sagua, M.A. Frechero, E. Matesanz, C. Leon, and E. Morán: Structure and physical properties of nickel manganite $NiMn_2O_4$ obtained from nickel permanganate precursor. *J. Eur. Ceram. Soc.* **30**, 2617–2624 (2010). doi: 10.1016/j.jeurceramsoc.2010.04.032.
34. T. Xiao-Xia, A. Manthiram, and J.B. Goodenough: $NiMn_2O_4$ revisited. *J. Less-Common Met.* **156**, 357–368 (1989). doi: 10.1016/0022-5088(89)90431-1.

https://doi.org/10.1557/jmr.2016.92 Published online by Cambridge University Press

35. L. Weil, F. Bertaut, and L. Bochirol: Propriétés magnétiques et structure de la phase quadratique du ferrite de cuivre. *J. Phys. Radium* **11**, 208–212 (1950). doi: 10.1051/jphysrad:01950001105020800.
36. A.A. Birajdar, S.E. Shirsath, R.H. Kadam, S.M. Patange, D.R. Mane, and A.R. Shitre: Rietveld structure refinement and cation distribution of Cr. *ISRN Ceram.* **2012**, 5 (2012). doi: 10.5402/2012/876123.
37. F. Chekin, H. Tahermansouri, and M. Besharat: Nickel oxide nanoparticles prepared by gelatin and their application toward the oxygen evolution reaction. *J. Solid State Electrochem.* **18**, 747–753 (2014). doi: 10.1007/s10008-013-2313-y.
38. M.P. Yeager, D. Su, N.S. Marinković, and X. Teng: Pseudocapacitive NiO fine nanoparticles for supercapacitor reactions. *J. Electrochem. Soc.* **159**, A1598–A1603 (2012). doi: 10.1149/2.025210jes.
39. L. Trotochaud, J.K. Ranney, K.N. Williams, and S.W. Boettcher: Solution-cast metal oxide thin film electrocatalysts for oxygen evolution. *J. Am. Chem. Soc.* **134**, 17253–17261 (2012). doi: 10.1021/ja307507a.
40. J. Bao, X. Zhang, B. Fan, J. Zhang, M. Zhou, W. Yang, X. Hu, H. Wang, B. Pan, and Y. Xie: Ultrathin spinel-structured nanosheets rich in oxygen deficiencies for enhanced electrocatalytic water oxidation. *Angew. Chem., Int. Ed.* **127**, 7507–7512 (2015). doi: 10.1002/anie.201502226.
41. R.N. Singh, J.P. Singh, H. Nguyen Cong, and P. Chartier: Effect of partial substitution of Cr on electrocatalytic properties of towards -evolution in alkaline medium. *Int. J. Hydrogen Energy* **31**, 1372–1378 (2006). doi: 10.1016/j.ijhydene.2005.11.012.
42. R.N. Singh, J.P. Singh, B. Lal, M.J.K. Thomas, and S. Bera: New $NiFe_{2-x}Cr_xO_4$ spinel films for O_2 evolution in alkaline solutions. *Electrochim. Acta* **51**, 5515–5523 (2006). doi: 10.1016/j.electacta.2006.02.028.
43. P. Strasser, S. Koh, T. Anniyev, J. Greeley, K. More, C. Yu, Z. Liu, S. Kaya, D. Nordlund, H. Ogasawara, M.F. Toney, and A. Nilsson: Lattice-strain control of the activity in dealloyed core–shell fuel cell catalysts. *Nat. Chem.* **2**, 454–460 (2010). (http://www.nature.com/nchem/journal/v2/n6/suppinfo/nchem.623_S1.html).
44. M.M. Jakšić: Electrocatalysis of hydrogen evolution in the light of the Brewer—Engel theory for bonding in metals and intermetallic phases. *Electrochim. Acta* **29**, 1539–1550 (1984). doi: 10.1016/0013-4686(84)85007-0.
45. E. Brinley, K.S. Babu, and S. Seal: The solution precursor plasma spray processing of nanomaterials. *JOM* **59**, 54–59 (2007). doi: 10.1007/s11837-007-0090-8.

Supplementary Material

To view supplementary material for this article, please visit http://dx.doi.org/10.1557/jmr.2016.92.

https://doi.org/10.1557/jmr.2016.92 Published online by Cambridge University Press